한국기계가공학회지, 제20권, 제7호, pp. 33～40(2021.07) ISSN 1598-6721(Print)
Journal of the Korean Society of Manufacturing Process Engineers, Vol. 20, No. 7, pp. 33~40(2021.07) ISSN 2288-0771(Online)

https://doi.org/10.14775/ksmpe.2021.20.07.033

Investigation of the Influence of Radius and Corner Position on the Residual Stress Distribution in the Vicinity of the Repaired Region via Directed Energy Deposition by using Finite Element Analysis

Aliyev Alissultan*, Kwang-Kyu Lee*, Dong-Gyu Ahn*,#
*School of Mechanical Engineering, Chosun UNIV.

유한 요소 해석을 이용한 DED 공정의 코너 반경 및 위치에 따른 보수 영역 부근 잔류응력 분포 영향성 조사

알리예브 알리술탄*, 이광규*, 안동규*,#
*조선대학교 기계공학과

(Received 02 June 2021; received in revised form 12 June 2021; accepted 17 June 2021)

ABSTRACT

Current industrial flow is directed toward reducing the usage of raw materials by reusing parts, which is referred to as a circular economy (CE). Repair is one of the most value-added approaches in CE, which can be efficiently accomplished via additive manufacturing. The repair technology of metallic parts via the directed energy deposition process, which includes the selective removal and redeposition of damaged regions of metallic parts. Residual stress characteristics depend on the shape of the part and the shape of the redeposition region. The objective of this study is to investigate the effects of the radius and corner position of the substrate on the residual stresses for repair by using finite element analysis (FEA). The residual stress distribution of the 45° angle groove at the edge of the circular shape models on the outer and inner radii was analytically investigated. The analysis was accomplished using SYSWELD software by applying a moving heat source with defined material properties and cooling conditions integrated into the FEA model. The results showed a similar pattern of concentrated stress distribution for all models except the 40-mm and 60-mm radii, for which the maximum stress locations were different. The maximum residual stresses are high but lower than the yield strength, suggesting the absence of cracks and fractures due to residual stresses.

Keywords : Residual Stress (잔류응력), Directed Energy Deposition Process (에너지 제어형 용착 공정), Finite Element Analysis Force(유한요소 해석), Radius of Metal Part(금속 부분의 반경), Position of Corner(코너 위치)

1. Introduction

Currently, the industry is concentrated on new approaches in material management, whose main objective is to reduce the usage of raw materials by reusing materials from existing products, which is

Corresponding Author : smart@chosun.ac.kr
Tel: +82-62-230-7234, Fax: +82-62-230-7234

Copyright © The Korean Society of Manufacturing Process Engineers. This is an Open-Access article distributed under the terms of the Creative Commons Attribution-Noncommercial 3.0 License (CC BY-NC 3.0 http://creativecommons.org/licenses/by-nc/3.0) which permits unrestricted non-commercial use, distribution, and reproduction in any medium, provided the original work is properly cited.

referred to as a circular economy[1]. Repair is one of the common aspects of a circular economy, and its main goal is to extend the life of a product[1]. Repair is more resource-efficient than recycling[2] and is considered to be the most value-added strategy in resource management[3].

The implementation of additive manufacturing (AM) technology for metallic parts is the best strategy to overcome limitations and difficulties related to manual repairing[2]. The most commonly used AM technology for repairing is directed energy deposition (DED) technology that can restore damaged parts layer by layer[2].

Damage to valuable metallic parts occurs in the form of voids and cavities[3]. The repair process includes the removal of the damaged region with subsequent redeposition. Several studies have been conducted to investigate the properties of deposited clads with different geometries. In Song et al.'s study, the trapezoidal groove of 304 stainless steel was repaired using 316 stainless steel powder by laser cladding with subsequent alloying of the surface by WC powders[4]. Song et al. investigated the restoration of V-grooves on an AISI1045 substrate using stainless steel powders and analyzed the properties of the deposited clad using numerous tests[5].

Experiments by Pinkerton et al. repairing H13 steel by H13 steel powders of triangular and square geometry slot demonstrated poor adhesion between the deposited material and the substrate on the sides of the squire-geometry groove owing to the lack of fusion[6].

Thermo-mechanical finite element analysis (FEA) was performed to investigate the post-solidification deposition characteristics of the model, such as residual stress distribution, dislocations, distortion, and final microstructure, which are practical for industrial applications[7].

In this study, residual stress characteristics when repairing different radius arc-shaped parts by DED are analytically investigated. A total of eight models, of which four are inner radius ones and four are outer radius deposition ones with a corner angle of 45° were modeled. The heat source, thermal, and dimensional boundary conditions are described in the next section, and the results of the simulation are discussed in terms of the effective stress and 1st principal stress distribution, and the results are summarized.

2. Finite Element Analysis

2.1 Heat Source Model and Thermal Losses

The metal powder in the DED process is blown through the nozzle onto the substrate or previously deposited layer and melted with a highly concentrated heat source such as a laser-creating melt pool, and the deposited region is built upon solidification of the melted material[4-7,8-10].

Because thermo-mechanical analysis depends on temperature histories, the definition of the heat source model is crucial[11]. The real laser beam heat flux distribution was very close to the Gaussian distribution. The highest power density was at the center of the beam, and it exponentially decreased away from the center. At any plane perpendicular to the z-axis within the effective penetration depth (D_0), the heat flux can be described by Equation (1)[12]:

$$Q(x,\ y,z) = Q_0{}^*\exp\left(-\frac{(x-vt)^2+y^2}{16^*\left(r_e+\frac{r_i-r_e}{z_i-z_e}(z-z_e)\right)}\right) \quad (1)$$

where $Q(x,\ y,z)$, Q_0, r, r_i, r_e, z_e and z_i are the volumetric heat flux at any point within the heat source volume, the maximum heat flux density at the center of the beam, the radius of beam at the top surface, the radius of beam at the penetration depth, the z coordinate of the heat source at the top surface, and the z coordinate of the heat source at the penetration depth respectively.

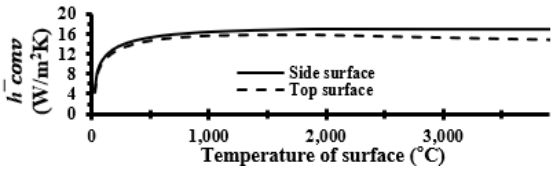

Fig. 1 Equivalent coefficient of natural convection

analysis involves long-time free air cooling as well as argon shielding. For more accurate simulation results, the average coefficient of the natural convection ($\overline{h}_{conv}$) based on temperature-dependent properties of argon and air was implemented into the model. Convection coefficient was estimated by Equation (2)[13]. The radiation coefficient $\overline{h}_{rad}$ can be calculated using Equation (3)[13].

$$\overline{h}_{conv} = \frac{N_L \cdot k}{L_c} \quad (2)$$

where NU_L, k, and L_c denote the average Nusselt number, thermal conductivity of the gas, and characteristic length of the specimen, respectively.

$$\overline{h}_{rad} = \epsilon\sigma_s\left(T_s^2 + T_\infty^2\right)\left(T_s + T_\infty\right) \quad (3)$$

where ϵ, σ_s, T_s and T_∞ are the emissivity of the material, the Stefan-Boltzmann constant, the surface temperature, and the ambient temperatures respectively.

For better efficiency of FEA, combined losses (q''_{loss}) from convection and radiation can be interpreted as a single Equation (4)[13]. The ambient and initial temperatures were set to 20°C. Fig. 1 shows the estimated equivalent coefficient of natural convection based on the temperature-dependent properties of air.

$$q''_{loss} = \left(\overline{h}_{conv} + \overline{h}_{rad}\right)\left(T_s - T_\infty\right) \quad (4)$$

2.2 Analysis Model

The temperature-dependent material properties of AISI 1045 were assigned to the substrate and deposition models for more accurate FEA results. Temperature-dependent material properties of AISI1045 were obtained from JmatPro software[14]. A total of eight models with eight beads for each model were created with deposition overlap assumed to be 33%. A schematic representation of FEA models is shown in Fig. 2, including revolve angle (θ), radius of curvature (R_{in}, R_{out}), and groove location and corner angle of the groove (β°). β° is equal to 45° for all models, while each model has a different θ° according to R_{in} and R_{out} so that each one has an approximately 30 mm outer bead. The value of θ for each radius of the model is shown in Fig. 3. Tables 1 and 2 list the bead lengths for each model.

To reduce the computational time and preserve the accuracy of the results, a fine mesh was generated only for deposition beads and the surrounding regions due to intensive heat flux and high temperatures in these regions. A biased mesh was mapped around the high heat flux region. Mesh generation and FEA were performed using a commercial software SYSWELD[12]. The inner radius deposition model shown in Fig. 4

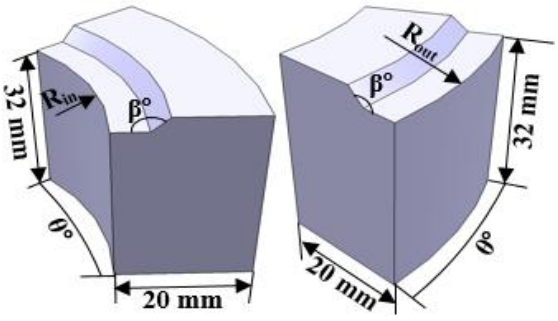

Fig. 2 Schematics of FEA models

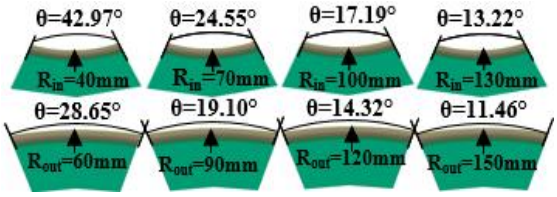

Fig. 3 Radius and θ ° of FEA models

Table 1 Bead lengths for inner radius side deposition

Radius			
40 mm	70 mm	100 mm	130 mm
Bead length (mm)			
31.57	30.89	30.63	30.48
30.68	30.37	30.27	30.20
31.80	31.01	30.72	30.55
30.89	30.51	30.36	30.27
30.00	29.99	30.00	30.00
32.47	31.41	30.99	30.76
31.57	30.90	30.63	30.48
30.68	30.37	30.27	30.20

Table 2 Bead lengths for outer radius side deposition

Radius			
60 mm	90 mm	120 mm	150 mm
Bead length (mm)			
28.95	29.31	29.47	29.59
29.55	29.71	29.77	29.83
28.80	29.20	29.39	29.52
29.40	29.60	29.69	29.76
30.00	30.00	29.99	30.00
28.36	28.91	29.17	29.35
28.95	29.31	29.47	29.59
29.55	29.71	29.77	29.83

summarizes the dimensional and thermal boundary conditions of the models. The outer radius deposition model has the same dimensions, except that the deposition region is on the outer side.

This study focuses on the FEA model and numerical analysis. In the future, an explicit experiment will be required for further optimization and validation of the FEA model. The width (W) and height (H) of the bead and other parameters such as the power of the laser (P), scan speed (V), and efficiency (η) were taken from the experimental results of deposition of single bead AISI1045 on AISI1045 substrate using DED machine DABO-300 (MAXROTEC) and shown in Table 3. Alternative direction deposition strategy was used for the analysis[9,10].

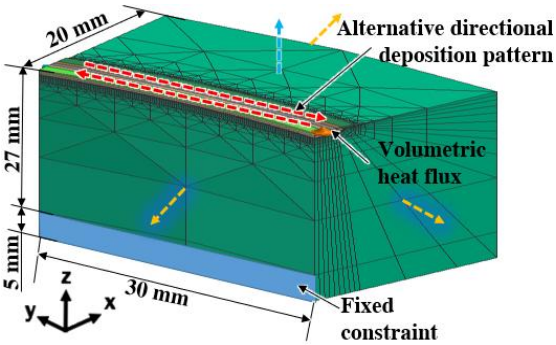

Fig. 4 Thermal and dimensional boundary conditions

Table 3 Analysis parameters

W (mm)	H (mm)	P (W)	V (mm/min)	η (%)
1.8	0.3	1000	800	34

3. Results and Discussions

3.1 Residual Stress Distribution of Repaired Inner Radius Side

Small volume depositions of three layers with eight beads in each model were analyzed. The results of the thermo-mechanical analysis in SYSWELD provide data on the post-solidification deposition characteristics of the models, including the stress distribution, displacement, and final microstructure. Fig. 5 shows the

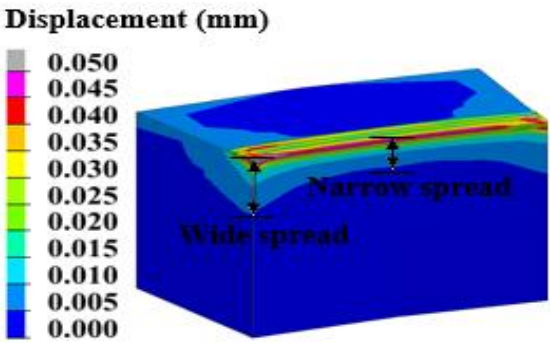

Fig. 5 Displacement distribution for inner radius side deposition

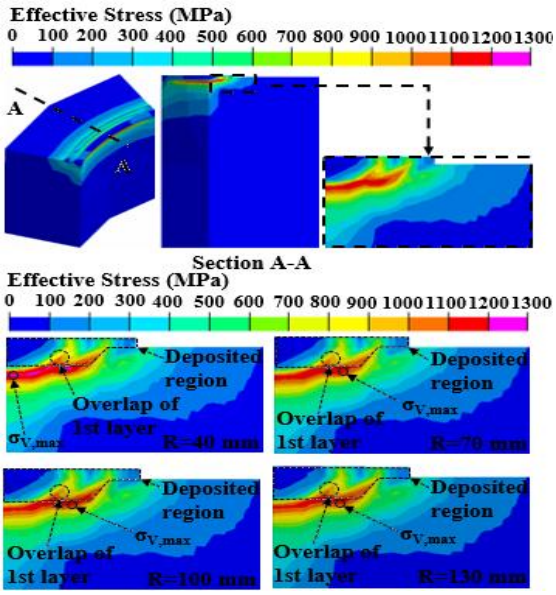

Fig. 6 Effective stress distribution for the cut through section A-A for inner radius side deposition

typical displacement at the end of cooling for the deposition of the inner radius side. Maximum displacement was observed at the edges of the deposition. This is because the displacement in that region was not restrained as much. In addition, destructive tests for residual stress evaluation are based on strain release by cutting metal specimens, indicating that the stressed regions of metal are constrained from dislocations[15]. Hence, regions with a high displacement show lower residual stresses. According to the FEA results, the displacement is widely spread throughout the volume of the models at the sides and tends to decrease toward the center. This indicates higher stresses at the center region; hence, the center section was selected to analyze the stress distribution.

The results of the analysis show an almost symmetrical distribution of the effective stress and 1st principal stress in all FEA models at the end of cooling. This is due to zero stress initial conditions and the use of an alternative direction deposition strategy [10,13]. From the observation of residual stresses for the cut through the center section for the distribution of concentrated

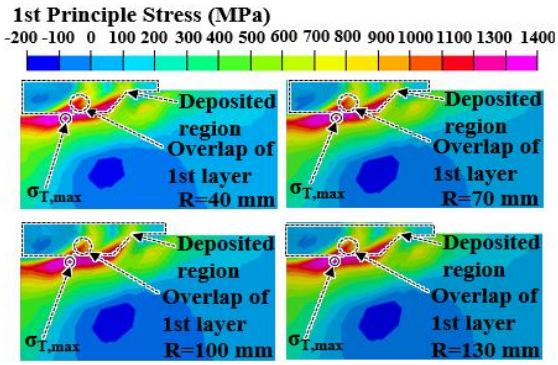

Fig. 7 1st principal stress distribution for the cut through section A-A for inner radius side deposition

effective stress and 1st principal tensile stress, a similar pattern is observed irrespective of the radius of deposition, as shown in Figs. 6 and 7, respectively. Concentrated residual stresses were observed under the deposition corner and extended from there until the outer surface below the deposition beads. Furthermore, the stresses spread in the overlap of the beads in the first layer and along the inclination at the corner.

The compressive 1st principle stress is at a certain distance from the deposition region, as demonstrated in Fig 7. Tensile and residual stresses must balance each other in equilibrium. A similar location of maximum effective stress ($\sigma_{v,max}$) under the 1st bead is applicable for all models except the 40-mm radius model, which has the maximum effective stress located on the surface under the deposition region, as shown in Fig. 6.

3.2 Residual Stress Distribution of Repaired Outer Radius Side

Fig. 8 shows the typical displacement distribution for the outer radius deposition case. Similarly, a higher displacement indicates higher stresses at the center. Hence, cutting through the center section was used for the analysis of stress distribution. A similar pattern for the effective and 1st principal stresses as in the inner radius side deposition observed in the outer radius side deposition, as shown in Figs. 9 and 10.

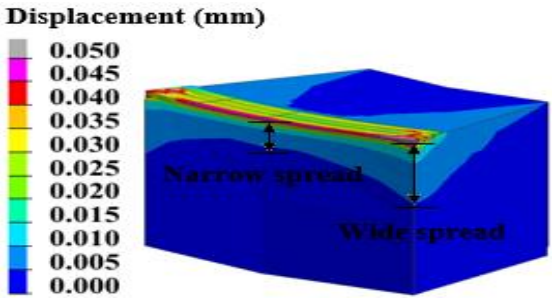

Fig. 8 Displacement distribution for outer radius side deposition

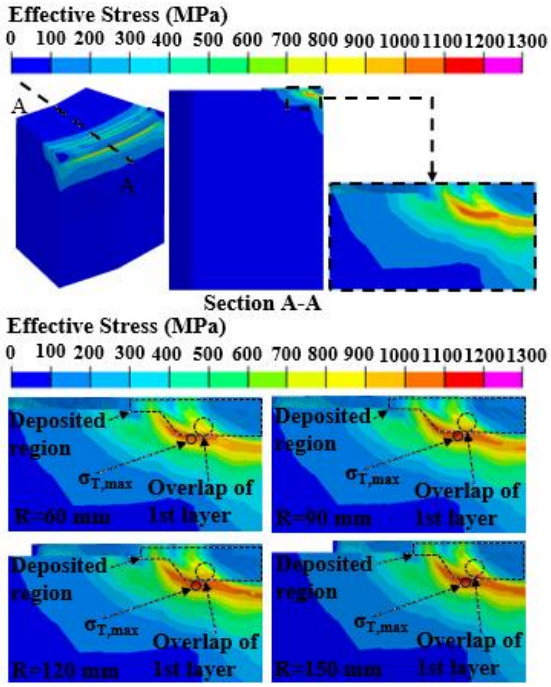

Fig. 9 Effective stress distribution for the cut through section A-A for outer radius side deposition

Highly concentrated stress were observed under the deposition beads and in the overlap of beads in the first layer. Starting from the corner until the outer surface was below the deposition region. However, for the outer radius deposition case, the overlap region and inclination at the corner were affected to a considerably lesser extent. Location of maximum principal stress ($\sigma_{v,max}$) is similar for all models except the 60 mm

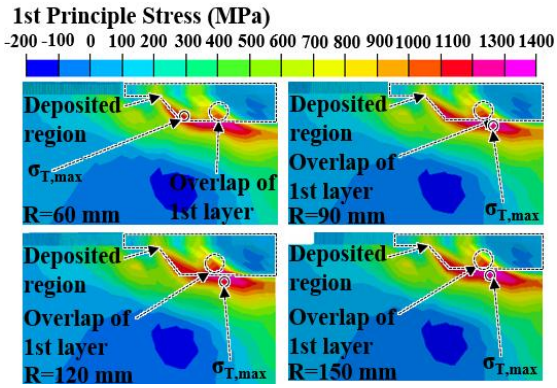

Fig. 10 1st principal stress distribution for the cut through section A-A for outer radius side deposition

radius model, which has maximum stresses at the corner. The magnitude of stress at the corner of the groove is high for all models; however, for a larger radius, the tensile 1st principal stress is predominant at the location under the overlap of the first layer.

3.3 Maximum Stress

At the end of 1 h of cooling, the temperatures of the models were at 35 °C-37 °C. The results of the simulation show that the deposited region underwent transformation to the martensitic phase. This is caused by heat dissipation from the deposited beads to the rest of the body through conduction, which contributed to the quenching effect[6]. The yield strength or fracture strength in the case of brittle martensite was 1,804 MPa at 50 °C[14]. The range of maximum 1st principal stress was 1,416-1,498 MPa for R_{in} and 1,255-1,321 MPa for R_{out}. The effective stress ranges are between 1,191-1,234 MPa and 1,091-1,126 MPa for R_{in} and R_{out}, respectively.

While a direct relation between radius size and thermal residual stresses was not observed, the smallest radii of analysis demonstrated exceptional results. In the outer radius side deposition case, the thermal residual stresses are considerably lower. In the case of a 60-mm radius, the lowest stresses are observed.

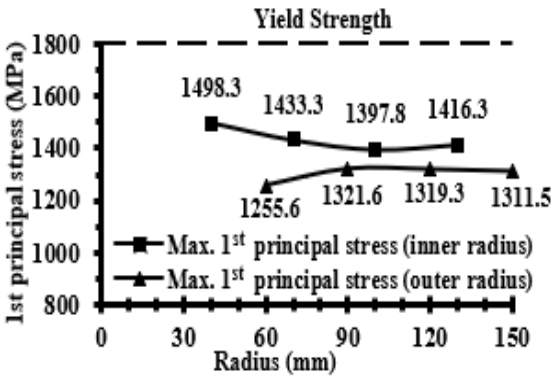

Fig. 11 Maximum 1st principal stresses for different corner radii and revolved angles

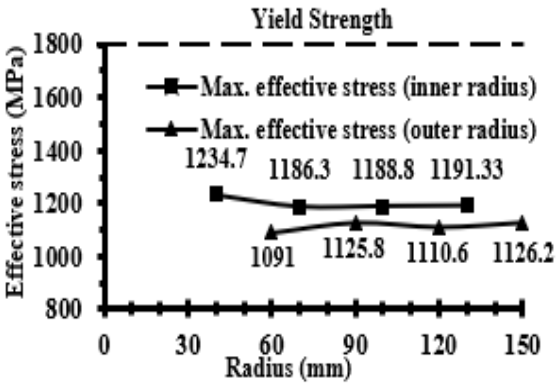

Fig. 12 Maximum effective stresses for different corner radii and revolved angles

However, in the inner radius deposition case, the smallest radius model of 40 mm showed the highest stresses. Therefore, a further investigation of residual stress for the reparation of the inner radius side by DED for small radius parts is necessary. All models show both maximum effective and 1st principal stresses lower than the yield strength, as shown in Figs. 11 and 12. From this result, it can be concluded that cracks or fractures are not likely to occur.

4. Conclusion

In this study, we analytically investigated the residual stress characteristics according to the radius of deposition and corner location during the repairing process by DED. From the results of the analysis, the following conclusions can be drawn:

1. When the inner radius of the metal part is repaired by DED, the location of the maximum stress concentration appears closer to the surface under the deposition clad for small radius parts.
2. After repairing the outer side of the round part, the maximum thermal residual stress is at the corner of the groove when the radius of the part is small. However, a small radius tends to exhibit lower stresses overall.
3. The maximum residual stresses at the end of cooling were considerably higher for the inner side deposition parts. Although the residual stress is in the range lower than the yield strength for all models, further investigation on the magnitudes of residual stress after repairs is needed for parts smaller than 40 mm.
4. The metal fracture behavior is influenced by residual stresses and can be the reason for fractures at considerably low applied stresses. Other negative effects of residual stresses include fatigue failure and lower corrosion resistance[15]. In future works, other repair strategies need to be considered, such as different inclination angles and, instead of sharp corners, the effect of grooves with different radius filets can be investigated.

Acknowledgement

This study was supported by the “Advanced remanufacturing of industrial machinery based on domestic CNC and building infrastructure for remanufacturing industry” of the Korea Institute of Energy Technology Evaluation and Planning (KETEP) granted financial resources from the Ministry of Trade, Industry & Energy, Republic of Korea (No. 20206310200010).

References

1. Reike, D., Vermeulen, W. J., Witjes, S., "The Circular Economy: New or Refurbished as CE 3.0?—Exploring Controversies in the Conceptualization of the Circular Economy through a Focus on History and Resource Value Retention Options," Resources, Conservation and Recycling, Vol. 135, pp. 246–264, 2018
2. Rahito; Wahab, D. A.; Azman, A. H., "Additive Manufacturing for Repair and Restoration in Remanufacturing: An Overview from Object Design and Systems Perspectives," Processes, Vol. 7, No. 11, pp. 802, 2019.
3. Wilson, J. M., Piya, C., Shin, Y., Zhao, F., Ramani, K., "Remanufacturing of turbine blades by laser direct deposition with its energy and environmental impact analysis," Journal of Cleaner Production, Vol. 80, pp. 170–178, 2014.
4. Song, L., Zeng, G., Xiao, H., Xiao, X., Li, S., "Repair of 304 stainless steel by laser cladding with 316L stainless steel powders followed by laser surface alloying with WC powders," Journal of Manufacturing Processes, Vol. 24, pp. 116–124, 2016.
5. Song, J., Deng, Q., Chen, C., Hu, D., Li, Y., "Rebuilding of metal components with laser cladding forming," Applied Surface Science, Vol. 252, pp. 7934–7940, 2006.
6. Pinkerton, A., Wang, W., Li, L., "Component repair using laser direct metal deposition," Proceedings of the Institution of Mechanical Engineers, Part B: Journal of Engineering Manufacture, Vol. 222, pp. 827–836, 2008.
7. Ren, K., Chew, Y., Fuh, J. Y. H., Zhang, Y. F., Bi, G. J., "Thermo-mechanical analyses for optimized path planning in laser aided additive manufacturing processes," Materials & Design, Vol. 162, pp. 80–93, 2019.
8. Zhang, X., Li, W., Adkison, K.M., Frank, L., "Damage reconstruction from tri-dexel data for laser-aided repairing of metallic components," The International Journal of Advanced Manufacturing Technology, Vol. 96, pp. 3377–3390, 2018.
9. Lu, X., Chiumenti, M., Cervera, M., Li, J., Lin, X., Ma, L., Zhang, G., Liang, E., "Substrate design to minimize residual stresses in Directed Energy Deposition AM processes," Materials & Design, Vol. 202, article 109525, 2021.
10. Chua, B. L., Ahn, D. G., "Estimation Method of Interpass Time for the Control of Temperature during a Directed Energy Deposition Process of a Ti–6Al–4V Planar Layer," Materials, Vol 13, No. 21, Article 4935, 2020.
11. Hung, T. P., Shi, H. E., Kuang, J. H., "Temperature Modeling of AISI 1045 Steel during Surface Hardening Processes. Materials," Vol. 11, No. 10, pp. 1815, 2018.
12. Sysweld, Visual-Environment Version 15.5, ESI Group Inc. 2021.
13. Kim, H., Lee, K. K., Ahn, D. G., Lee, H., "Effects of Deposition Strategy and Preheating Temperature on Thermo-Mechanical Characteristics of Inconel 718 Super-Alloy Deposited on AISI 1045 Substrate Using a DED Process," Materials, Vol. 14, No. 7, Article 1794, 2021.
14. JmatPro, JmatPro version 12.0, Sente Software Ltd. 2021.
15. Jenney, C. L., O'Brien, A., Welding Handbook, Vol 1: Welding Science and Technology (9th ed.), Woodhead Publishing Ltd., pp 297–357, 2001.